

The unmixed kinematics and origins of diffuse stellar light in the core of the Hydra I cluster (Abell 1060)

G. Ventimiglia^{1,2}, M. Arnaboldi^{2,3}, and O. Gerhard¹

¹ Max-Planck-Institut für Extraterrestrische Physik, Giessenbachstraße 1, 85741 Garching bei München, Germany
e-mail: gventimi@mpe.mpg.de

² European Southern Observatory, Karl-Schwarzschild-Straße 2, 85748 Garching bei München, Germany

³ INAF, Osservatorio Astronomico di Pino Torinese, 10025 Pino Torinese, Italy

Received 22 October 2010 / Accepted 16 December 2010

ABSTRACT

Context. Diffuse intracluster light (ICL) and cD galaxy halos are believed to stem from galaxy evolution and disruption in clusters. **Aims.** The processes involved may be constrained by studying the dynamical state of the ICL and the galaxies in the cluster core. Here we present a kinematic study of diffuse light in the Hydra I (Abell 1060) cluster core, using planetary nebulae (PNs) as tracers. **Methods.** We used multi-slit imaging spectroscopy with FORS2 on VLT-UT1 to detect 56 PNs associated with diffuse light in the central $100 \times 100 \text{ kpc}^2$ of the Hydra I cluster, at a distance of $\sim 50 \text{ Mpc}$. We measured their [OIII] m_{5007} magnitudes, sky positions, and line-of-sight velocity distribution (LOSVD), and compared them with the phase-space distribution of nearby galaxies. **Results.** The luminosity function of the detected PNs is consistent with that expected at a distance of $\sim 50 \text{ Mpc}$. Their number density is ~ 4 times lower for the light seen than expected, and we discuss ram pressure stripping of the PNs by the hot intracluster medium as one of the possible explanations. The LOSVD histogram of the PNs is highly non-Gaussian and multi-peaked: it is dominated by a broad central component with $\sigma \sim 500 \text{ km s}^{-1}$ at around the average velocity of the cluster, and shows two additional narrower peaks at 1800 km s^{-1} and 5000 km s^{-1} . The main component is broadly consistent with the outward continuation of the intracluster halo of NGC 3311, which was earlier shown to have a velocity dispersion of $\sim 470 \text{ km s}^{-1}$ at radii of $\gtrsim 50''$. Galaxies with velocities in this range are absent in the central $100 \times 100 \text{ kpc}^2$ and may have been disrupted earlier to build this component. The PNs in the second peak in the LOSVD at 5000 km s^{-1} are coincident spatially and in velocities with a group of dwarf galaxies in the MSIS field. They may trace the debris from the ongoing tidal disruption of these galaxies. **Conclusions.** Most of the diffuse light in the core of Abell 1060 is still not phase-mixed. The build-up of ICL and the dynamically hot cD halo around NGC 3311 are ongoing, through the accretion of material from galaxies falling into the cluster core and tidally interacting with its potential well.

Key words. galaxies: clusters: general – galaxies: clusters: individual: hydra I – galaxies: elliptical and lenticular, cD – galaxies: individual: NGC 3311 – planetary nebulae: general

1. Introduction

Intracluster light (ICL) consists of stars that fill up the cluster space among galaxies and that are not physically bound to any galaxy cluster members. For clusters in the nearby universe, the morphology and quantitative photometry of the ICL have been studied with deep photometric data or by detection of single stars in large areas of sky.

Deep large-field photometry shows that ICL is common in clusters of galaxies and it has morphological structures with different angular scales. The fraction of light in the ICL with respect to the total light in galaxies is between 10% and 30%, depending on the cluster mass and evolutionary status (Feldmeier et al. 2004; Adami et al. 2005; Mihos et al. 2005; Zibetti et al. 2005; Krick & Bernstein 2007; Pierini et al. 2008). The detection of individual stars associated with the ICL, such as planetary nebulae (PNs) (Arnaboldi et al. 2004; Aguerri et al. 2005; Gerhard et al. 2007; Castro-Rodríguez et al. 2009), globular clusters (GCs) (Hilker 2002; Lee et al. 2010), red giants stars (Durrell et al. 2002; Williams et al. 2007), and supernovae (Gal-Yam et al. 2003; Neill et al. 2005) is a complementary approach to deep photometry for studying the ICL, also enabling kinematic measurements for this very low surface brightness population.

An important open question is the relation between the ICL and the extended outer halos of brightest cluster galaxies (BCGs), whether they are independent components or whether the former is a radial extension of the latter. Using a sample of 683 SDSS clusters, Zibetti et al. (2005) found a surface brightness excess with respect to an inner $R^{1/4}$ profile used to describe the mean profile of the BCGs, but it is not known yet whether this cD envelope is simply the central part of the cluster's diffuse light component or whether it is distinct from the ICL and part of the host galaxy (Gonzalez et al. 2005).

Both the ICL and the halos of BCGs are believed to have formed from stars that were tidally dissolved from their former host galaxies or from entirely disrupted galaxies. A number of processes have been discussed, starting with early work such as Richstone (1976); Hausman & Ostriker (1978). Contributions to the ICL are thought to come from weakly bound stars generated by interactions in galaxy groups, subsequently released in the cluster's tidal field (Rudick et al. 2006, 2009; Kapferer et al. 2010), interactions of galaxies with each other and with the cluster's tidal field (Moore et al. 1996; Gnedin 2003; Willman et al. 2004), and from tidal dissolution of stars from massive galaxies prior to mergers with the BCG (Murante et al. 2007; Puchwein et al. 2010). Stars in BCG halos may have originated in both such major mergers as well as through minor mergers with the

BCG. Which of these processes are most important is still an open issue.

Kinematic studies of the ICL and the cD halos are instrumental in answering these questions. The kinematics of the ICL contains the fossil records of past interactions, due to the long dynamical timescale, and thus helps in reconstructing the processes that dominate the evolution of galaxies in clusters and the formation of the ICL (Napolitano et al. 2003; Rudick et al. 2006; Gerhard et al. 2007; Murante et al. 2007; Arnaboldi & Gerhard 2010). The kinematics in the cD halos can be used to separate cluster from galaxy components, as shown in simulations (Dolag et al. 2010); so far, however, the observational results are not unanimous: in both NGC 6166 in Abell 2199 (Kelson et al. 2002) as well as NGC 3311 in Abell 1060 (Ventimiglia et al. 2010b) the velocity dispersion profile in the outer halo rises to nearly cluster values, whereas in the Fornax cD galaxy NGC 1399 (McNeil et al. 2010) and in the central Coma BCGs (Coccatto et al. 2010) the velocity dispersion profiles remain flat, and in M 87 in Virgo (Doherty et al. 2009) it appears to fall steeply to the outer edge. Evidently, more work is needed both to enlarge the sample and to link the results to the evolutionary state of the host clusters.

The aim of this work is to further study the NGC 3311 halo, how it blends into the ICL, and what is its dynamical status. NGC 3311 is the cD galaxy in the core of the Hydra I (Abell 1060) cluster. Based on X-ray evidence, the Hydra I cluster is the prototype of a relaxed cluster (Tamura et al. 2000; Furusho et al. 2001; Christlein & Zabludoff 2003). Surface photometry is available in the Johnson B, Gunn g and r bands (Vasterberg et al. 1991), and the velocity dispersion profile has been measured out to $\sim 100''$ (Ventimiglia et al. 2010b), showing a steep rise to $\sim 470 \text{ km s}^{-1}$ in the outer halo. Here we use the kinematics of PNs from a region of $100 \times 100 \text{ kpc}^2$ centered on NGC 3311, to extend the kinematic study to larger radii and characterize the dynamical state of the outer halo and of the cluster core.

In Sect. 2 we summarize the properties of the Hydra I cluster from X-ray and optical observations. In Sect. 3 we discuss PNs as kinematical and distance probes, and the “Multi-Slit Imaging Spectroscopy – MSIS” technique for their detection in clusters in the distance range 40–100 Mpc. We present the observations, data reduction, identification, and photometry in Sects. 4 and 5. In Sect. 6 we describe the spatial distribution, line-of-sight (LOS) velocity distribution (LOSVD), and magnitude-velocity plane of the PN sample. In Sect. 7 we use the properties of the planetary nebulae luminosity function (PNLF) and a kinematic model for the PN population to predict its LOSVD in MSIS observations. The simulation allows us to interpret the observed LOSVD and also to determine the luminosity-specific PN number or α parameter for the halo of NGC 3311. In Sect. 8 we correlate the velocity subcomponents in the PN LOSVD with kinematic substructures in the Hydra I galaxy distribution and discuss implications for galaxy evolution and disruption in the cluster core. Finally, Sect. 9 contains a summary and the conclusions of this work.

2. The Hydra I cluster of galaxies (Abell 1060)

The Hydra I cluster (Abell 1060) is an X-ray bright, non-cooling flow, medium compact cluster in the southern hemisphere, whose central region is dominated by a pair of non-interacting giant elliptical galaxies, NGC 3311 and NGC 3309. NGC 3309 is a regular giant elliptical (E3) and NGC 3311 is a cD galaxy with an extended halo (Vasterberg et al. 1991).

X-ray properties of Hydra I – Except for two peaks associated with the bright elliptical galaxies NGC 3311 and NGC 3309, the X-ray emission from the hot intracluster medium (ICM) in the Hydra I (A 1060) cluster is smooth and lacks prominent spatial substructures. The center of the nearly circularly symmetric emission contours roughly coincides with the center of NGC 3311 (Tamura et al. 2000; Yamasaki et al. 2002; Hayakawa et al. 2004, 2006). A faint extended emission with angular scale $< 1'$ trailing NGC 3311 to the northeastern, overlapping with an Fe excess, could be due to gas stripped from NGC 3311 if the galaxy moved towards the south-west with velocity $\gtrsim 500 \text{ km s}^{-1}$, according to Hayakawa et al. (2004, 2006). The total gas mass and iron mass contained in this region are $\sim 10^9 M_\odot$ and $2 \times 10^7 M_\odot$, respectively (Hayakawa et al. 2004, 2006). The emission components of NGC 3311 and NGC 3309 themselves are small, extending to only $\sim 10'' \approx 2.5 \text{ kpc}$, suggesting that both galaxies lost most of their gas in earlier interactions with the ICM. In both galaxies, the X-ray gas is hotter than the equivalent temperature corresponding to the central stellar velocity dispersions, and in approximate pressure equilibrium with the ICM (Yamasaki et al. 2002).

On cluster scales the X-ray observations show that the hot ICM has a fairly uniform temperature distribution, ranging from about 3.4 KeV in the center to 2.2 KeV in the outer region, and constant metal abundances out to a radius of 230 kpc. Deviations from uniformity of the hot gas temperature and metallicity distribution in Hydra I are in the high metallicity region at ~ 1.5 arcmin northeastern of NGC 3311, and a region at a slightly higher temperature at 7 arcmin south-east of NGC 3311 (Tamura et al. 2000; Furusho et al. 2001; Yamasaki et al. 2002; Hayakawa et al. 2004, 2006; Sato et al. 2007). Based on the overall regular X-ray emission and temperature profile, the Hydra I cluster is considered as the prototype of an evolved and dynamically relaxed cluster, with the time elapsed since the last major sub-cluster merger being at least several Gyr. From the X-ray data the central distribution of dark matter in the cluster has been estimated, giving a central density slope of $\simeq -1.5$ and a mass within 100 kpc of $\simeq 10^{13} M_\odot$ (Tamura et al. 2000; Hayakawa et al. 2004). Given these properties, the Hydra I cluster is an interesting target for studying the connection between the ICL and the extended halo of NGC 3311.

The cluster average velocity and velocity dispersion – From a deep spectroscopic sample of cluster galaxies extending to $M_R \leq -14$, Christlein & Zabludoff (2003) derive the average cluster redshift (mean velocity) and velocity dispersion of Hydra I. We adopt their values here: $\bar{v}_{\text{Hy}} = 3683 \pm 46 \text{ km s}^{-1}$, and $\sigma_{\text{Hy}} = 724 \pm 31 \text{ km s}^{-1}$. The sample of measured galaxy spectra in Hydra I is extended to fainter magnitudes $M_V > -17$ through the catalog of early-type dwarf galaxies published by Misgeld et al. (2008); their values for the average cluster velocity and velocity dispersion are $\bar{v}_{\text{Hy}} = 3982 \pm 148 \text{ km s}^{-1}$ and $\sigma_{\text{Hy}} = 784 \text{ km s}^{-1}$, with the average cluster velocity at somewhat higher value with respect to the measurement by Christlein & Zabludoff (2003). Both catalogs cover a radial range of $\sim 300 \text{ kpc}$ around NGC 3311. Close to NGC 3311, a predominance of velocities redshifted with respect to \bar{v}_{Hy} is seen, but in the radial range ~ 50 – 300 kpc , the velocity distribution appears well-mixed with about constant velocity dispersion.

Distance estimates – The distance to the Hydra I cluster is not well constrained yet, as different techniques provide rather different estimates. The cosmological distance to Abell 1060 based on the cluster redshift is $51.2 \pm 5.7 \text{ Mpc}$ assuming $H_0 = 72 \pm 8 \text{ km}^{-1} \text{ Mpc}^{-1}$ (Christlein & Zabludoff 2003), while direct

measurements using the surface brightness fluctuation (SBF) method for 16 galaxies give a distance of 41 Mpc (Mieske et al. 2005).

The relative distance of NGC 3311 and NGC 3309 along the line of sight is also controversial. Distance measurements based on the globular cluster luminosity function locate NGC 3311 about 10 Mpc in front of NGC 3309, which puts NGC 3309 at 61 Mpc (Hilker 2003), while SBF measurements suggest the opposite, with NGC 3311 now at shorter distance of about 41 Mpc and NGC 3309 even closer at 36 Mpc, 5 Mpc in front of NGC 3311 (Mieske et al. 2005).

In this work we assume a distance for NGC 3311 and the Hydra I cluster of 51 Mpc, corresponding to a distance modulus of 33.54. Then $1''$ corresponds to 0.247 kpc. The systemic velocity for NGC 3311 and its central velocity dispersion are $v_{N3311} = 3825 (3800) \pm 8 \text{ km s}^{-1}$ (heliocentric; without and in brackets with relativistic correction), and $\sigma_0 = 154 \pm 16 \text{ km s}^{-1}$ (Ventimiglia et al. 2010b). The systemic velocity of NGC 3309 is $v_{N3309} = 4099 \text{ km s}^{-1}$ (Misgeld et al. 2008). The velocities of the other Hydra I galaxies are extracted from the catalogs of Misgeld et al. (2008) and Christlein & Zabludoff (2003).

3. Probing the ICL kinematics using planetary nebulas

3.1. Planetary nebulas as kinematical probes and distance indicators

PNs occur as a brief phase during the late evolution of solar-type stars. In stellar populations older than 2 Gyr, about one star every few million is expected to be in the PN phase at any one time (Buzzoni et al. 2006). Stars in the PN phase can be detected via their bright emission in the optical [OIII] λ 5007 Å emission line, because the nebular shell re-emits $\sim 10\%$ of the UV photons emitted by the stellar core in this single line (Ciardullo et al. 2005). When the [OIII] emission line is detected, the line-of-sight velocity of the PN can be easily measured.

The number density of PNs traces the luminosity density of the parent stellar population. According to single stellar population theory, the luminosity-specific stellar death rate is independent of the precise star formation history of the associated stellar population (Renzini & Buzzoni 1986; Buzzoni et al. 2006). This property is captured in a simple relation such that

$$N_{\text{PN}} = \alpha L_{\text{gal}} \quad (1)$$

where N_{PN} is the number of all PNs in a stellar population, L_{gal} is the bolometric luminosity of that parent stellar population and α is the luminosity-specific PN number. The predictions from stellar evolution theory are further supported by empirical evidence that the PN number density profiles follow light in late- and early-type galaxies (Herrmann et al. 2008; Coccato et al. 2009), and that the luminosity-specific PN number α stays more or less constant with $(B - V)$ color. The empirical result that the rms scatter of α for a given color is about a factor 2–3 remains to be explained, however (Buzzoni et al. 2006).

The planetary nebula luminosity function (PNLF) technique is one of the simplest methods for determining extragalactic distances. This is based on the observed shape of the PNLF. At faint magnitudes, the PNLF has the power-law form predicted from models of uniformly expanding shells surrounding slowly evolving central stars (Henize & Westerlund 1963; Jacoby 1980). However, observations and simulations have demonstrated that the bright end of the PNLF dramatically breaks from

this relation and falls to zero very quickly, within ~ 0.7 mag (Ciardullo et al. 1998; Mendez & Soffner 1997). It is the constancy of the cutoff magnitude, $M^* = -4.51$, and the high monochromatic luminosity of PNs, that makes the PNLF such a useful standard candle.

3.2. The multi-slit imaging spectroscopy technique

At the distance of the Hydra I cluster, the brightest PNs at the PNLF cutoff have an apparent m_{5007} magnitude equal to 29.0, corresponding to a flux in the [OIII] λ 5007 Å line of $\sim 8 \times 10^{-18} \text{ erg s}^{-1} \text{ cm}^{-2}$ according to the definition of m_{5007} by Jacoby (1989). To detect these faint emissions we need a technique that substantially reduces the noise from the night sky. This is possible by using a dedicated spectroscopic technique named “Multi-Slit Imaging Spectroscopy” (MSIS, Gerhard et al. 2005; Arnaboldi et al. 2007).

MSIS is a blind search technique that combines the use of a mask of parallel slits, a dispersing element, and a narrow band filter centered at the redshifted [OIII] λ 5007 Å emission line. With MSIS exposures, PNs and other emission objects in the filter’s wavelength range which happen to lie behind the slits are detected, and their velocities, positions, and magnitudes can be measured at the same time. The [OIII] emission line from a PN is $\sim 30 \text{ km s}^{-1}$ wide (Arnaboldi et al. 2008), so if dispersed with a spectral resolution $R \sim 6000$, it falls on a small number of pixels, depending on the slit width and seeing.

In this work we use MSIS to locate a sample of PNs in the core of the Hydra I cluster and measure their velocities and magnitudes. Our aim is to infer the dynamical state of the diffuse light in the cluster core, as described below in Sects. 7 and 8.

4. Observations

MSIS data for Hydra I were acquired during the nights of March 26–28, 2006, with FORS2 on UT1, in visitor mode. The FORS2 field-of-view (FoV) is $\sim 6.8 \times 6.8 \text{ arcmin}^2$, corresponding to $\sim 100 \times 100 \text{ kpc}^2$ at the distance of the Hydra I cluster. The effective field area in which it was possible to position slits with the Grism used here is 44.6 arcmin^2 . The FoV was centered on NGC 3311 at $\alpha = 10^{\text{h}}36^{\text{m}}42.8^{\text{s}}$, $\delta = -27^{\text{d}}31^{\text{m}}42^{\text{s}}$ (J2000) in the core of the cluster. The FoV is imaged onto two 2×2 rebinned CCDs, with spatial resolution $0''.252$ per rebinned-pixel. The mask used has 24×21 slits, each $0''.8$ wide and $17''.5$ long. The area covered with the mask is about 7056 arcsec^2 , corresponding to about 4.4% of the effective FoV. To cover as much of the field as possible, the mask was stepped 15 times so as to fill the distance between two adjacent slits in the mask. The total surveyed area is therefore 29.4 arcmin^2 , i.e., 66% of the effective FoV. Three exposures of 800 s were taken at each mask position to facilitate the removal of cosmic rays during the data reduction process.

The dispersing element was GRISM-600B with a spectral resolution of $0.75 \text{ Å pixel}^{-1}$ (or $1.5 \text{ Å rebinned-pixel}^{-1}$) at 5075 Å . With the adopted slit width, the measured spectral resolution is 4.5 Å or 270 km s^{-1} . Two narrow band filters were used, centered at 5045 Å and 5095 Å , respectively, both with 60 Å FWHM . This ensures the full coverage of the Hydra I cluster LOS velocity range. Each illuminated slit in the mask produces a two-dimensional spectrum of 40 rebinned pixels in the spectral direction and 70 rebinned pixels in the spatial direction.

The seeing during the observing nights was in the range from $0''.6$ to $1''.5$. For the average seeing ($0''.9$) and with the spectral

resolution of the set-up, monochromatic point-like sources appear in the final spectra as sources with a total width of ~ 5 pixels in both the spatial and wavelength directions.

Biases and through-mask flat field images were also taken. Arc-lamp calibration frames with mask, Grism and narrow band filter were acquired for the extraction of the 2D spectra, their wavelength calibration and distortion correction. Long slit data for the standard star LTT 7379 with narrow band filter and Grism were acquired for flux calibration.

5. Data reduction and analysis

The data reduction is carried out in *IRAF* as described in [Arnaboldi et al. \(2007\)](#) and [Ventimiglia et al. \(2008\)](#). The frames are registered and co-added after bias subtraction. The continuum light from the bright galaxy halos is subtracted using a median filtering technique implemented in the *IRAF* task *.images.imfilter.median*, with a rectangular window of 19×35 pixels. Then emission line objects are identified, and 2D-spectra around the emission line positions are extracted, rectified, wavelength and flux calibrated, and background subtracted. Finally the wavelength of the redshifted [OIII] λ 5007 Å emission line for all the identified sources is measured via a Gaussian fit. The heliocentric correction for the PN velocities is -5.44 km s^{-1} .

5.1. Identification of emission-line objects

All emission line objects found are classified according to the following criteria as

- PN candidates: unresolved emission line objects, both in wavelength and spatial direction, with no continuum;
- background galaxy candidates: unresolved emission line objects with continuum or resolved emission line objects both with and without continuum.

The total number of detected emission line sources in our data set is 82, of which 56 are classified as PN candidates and 26 as background galaxy candidates, of which 6 are classified as [OII] emitters and the remaining 20 as candidate Ly α galaxies¹.

For details on the background galaxy candidates see [Ventimiglia et al. \(2010a\)](#). Note that the background galaxy classification is independent of luminosity and that these objects have a broad equivalent width distribution. Therefore, the fact that the PN candidates (unresolved emission line objects without detectable continuum) have a luminosity function as expected for PNs observed with MSIS at a distance of ~ 50 Mpc (see Sect. 7.1), implies that the large majority of these PN candidates must indeed be PNs. In addition, Fig. 1 of [Ventimiglia et al. \(2010a\)](#) shows that all of the background galaxy candidates but two fall in the blue filter in the velocity range between 1000 km s^{-1} and 2800 km s^{-1} , blue-shifted with respect to the Hydra I cluster. Several of the *unresolved* background galaxies in this blue-shifted velocity range have a continuum level just above the detectability threshold, suggesting that the PN candidate sample may contain a few background galaxy contaminants in this velocity range whose continuum is too faint to detect.

¹ Note that the equivalent widths (*EWs*) of the PN candidates are mostly distributed between $30 \text{ \AA} < EW < 100 \text{ \AA}$, similar to the *EWs* of the background galaxy candidates, and cannot therefore be used to discriminate between both types of emission sources. This is because these distant PNs are faint and the continuum level in the MSIS images is given by the 1σ limit from the sky noise; see Sect. 5.2.

The two background galaxies seen in the red filter are both extended and have medium bright emission fluxes; one has a very bright continuum, the other no detectable continuum. From this we conclude that the residual contamination of the PN candidate sample at velocities $> 3000 \text{ km s}^{-1}$ must be minimal. With this in mind, we will in the following simply refer to the PN candidates as PNs.

5.2. Photometry

Magnitudes of the PN candidates are computed using the m_{5007} definition by [Jacoby \(1989\)](#), $m_{5007} = -2.5 \log F_{5007} - 13.74$, where F_{5007} is the integrated flux in the line computed in circular apertures of radius $0'.65$ – $0'.85$ in the 2D spectra, measured using the *IRAF* task *.noao.digiphot.aphot.phot*. The 1σ limit on the continuum in these spectra is $7.2 \times 10^{-20} \text{ erg cm}^{-2} \text{ s}^{-1} \text{ \AA}^{-1}$.

5.2.1. Photometric errors and completeness function

The photometric errors are estimated using simulations on a sample of 2D wavelength, flux calibrated and background subtracted spectra. For each simulation 100 artificial PN sources are generated using the *IRAF* task *.noao.artdata.mkobject*. The adopted PSF is a Gaussian with a dispersion obtained by fitting a 2D Gaussian to the profile of a detected PN candidate with adequate signal-to-noise. The σ value is 1.1 pixels, i.e., $FWHM \sim 0'.7$, and the $FWHM$ in wavelength is $\sim 4 \text{ \AA}$. The simulated PN samples have luminosity functions (LFs) given by a delta function at one of five different input magnitudes (29.3, 29.7, 30.1, 30.5 and 30.9 mag). The output magnitudes on the 2D spectra are measured with *.noao.digiphot.aphot.phot* using circular apertures, in the same way as for real PN candidates. In these experiments, no significant systematic shift in the magnitudes was found, and the standard deviation of the retrieved magnitude distribution is adopted as the measured error at the respective *output* magnitude.

On the basis of these simulations, we thus model the errors for the MSIS m_{5007} photometry, which increase approximately linearly towards fainter magnitudes, by

$$\epsilon \simeq 0.25(m_{5007} - 28.5) [29.0, 30.4]. \quad (2)$$

We then evaluate a completeness correction function, using the fraction of objects retrieved at each magnitude as these become fainter. This fraction is nearly 100% at 29.0 mag, the apparent magnitude of the PNLF bright cutoff at 51 Mpc, and decreases linearly down to 10–20% at 30.4 mag, the detection limit magnitude of our observations. We model this dependence by

$$f_c \simeq \begin{cases} 1 & \text{if } m_{5007} \leq 29.0, \\ 0.64(-m_{5007} + 30.55) & \text{if } 29.0 < m_{5007} \leq 30.4, \\ 0 & \text{if } m_{5007} > 30.4. \end{cases} \quad (3)$$

The error distribution and the completeness function are used in Sect. 7 below to perform simulations of the LOSVD for the PN sample.

6. The PN sample in Hydra I

Our PN catalog for the central (100 kpc)² of the Hydra I cluster contains 56 candidates, for which we measure v_{LOS} , x_{PN} , y_{PN} and m_{5007} . The detected PN velocities cover a range from 970 km s^{-1} to 6400 km s^{-1} with fluxes from $2.2 \times 10^{-18} \text{ erg cm}^{-2} \text{ s}^{-1}$ to $7.6 \times 10^{-18} \text{ erg cm}^{-2} \text{ s}^{-1}$. The detected sample of objects have

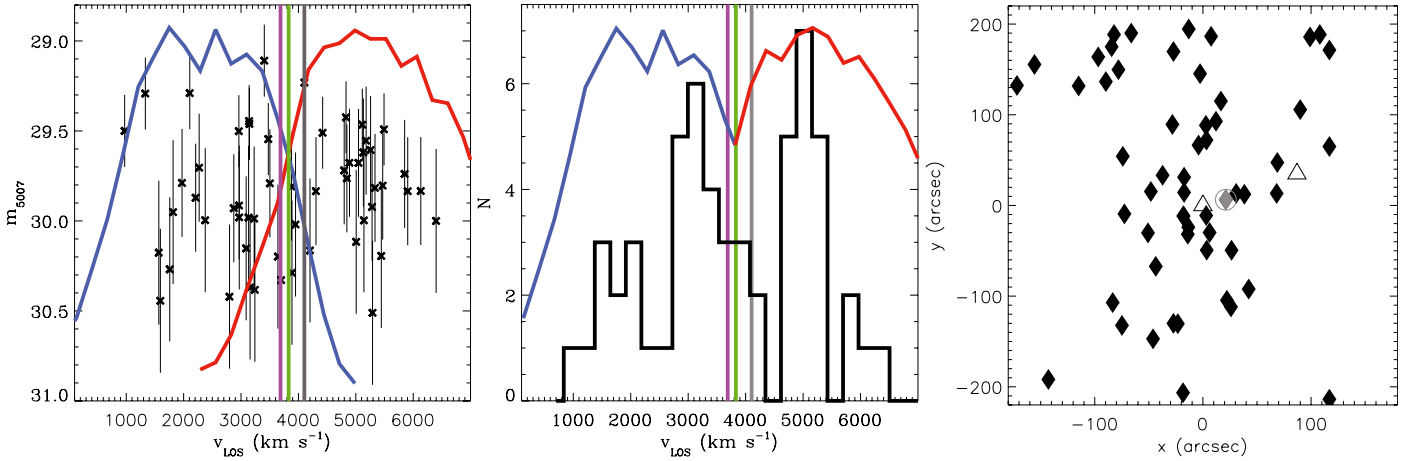


Fig. 1. PNs in the Hydra I cluster core. *Left panel:* the PN velocity-magnitude distribution. The black crosses show the entire sample of 56 PN candidates. The blue and red lines are the measured transmission curves of the blue and the red filter, respectively, normalized so that the maximum transmission is near the theoretical bright cutoff of the PNLF at the distance of Hydra I. *Central panel:* the PN LOSVD (black histogram). The bins in velocity are 270 km s^{-1} wide. The blue and the red solid lines show again the suitably normalized transmission curves of the blue and red filters. The vertical magenta, green and gray lines in both panels mark the systemic velocity of Hydra I, NGC 3311 and NGC 3309, respectively. *Right panel:* spatial distribution of the PNs (black diamonds) in the MSIS field. The field is centered on NGC 3311 and has size $\sim 100 \times 100 \text{ kpc}^2$; north is up and east to the left. The two open triangles indicate the positions of NGC 3311 (*center*) and NGC 3309 (*upper right*). The PN indicated by the gray symbol is the only object compatible with a PN bound to NGC 3309, based on its position on the sky and LOS velocity, $v_{\text{grayPN}} = 4422 \text{ km s}^{-1}$.

a magnitude distribution compatible with the PNLF at the distance of Hydra I; see also Sect. 7.1.

The magnitude-velocity plane – The properties of the PN sample in the velocity-magnitude plane are shown in the left panel of Fig. 1². In this plot, the apparent magnitude of the PNLF bright cutoff at the distance of the Hydra I cluster corresponds to a horizontal line at 29.0 mag. The blue and red lines are the filter transmission curves, as measured from the spectra, normalized so that the maximum transmission occurs near the PNLF bright cutoff. The PNs are indeed all fainter than $m_{5007} = 29.0$ and extend to the detection limit magnitude, m_{dl} . This is slightly different for the two filters; the faintest PNs detected through the blue filter have $m_{B,\text{dl}} = 30.45$, and those detected with the red filter have $m_{R,\text{dl}} = 30.3$.

The PN LOSVD – The measured LOSVD of the PN sample is shown by the black histogram in the central panel of Fig. 1. The velocity window covered by the two filters is also shown and the systemic velocities of Hydra I, NGC 3311 and NGC 3309 (see Sect. 2) are indicated by the magenta, green and gray vertical lines, respectively. These velocities fall in the middle of the velocity window allowed by the filters, where both filters overlap. The mean velocity of all PN candidates is $\bar{v}_{\text{PNs}} = 3840 \text{ km s}^{-1}$ and the standard deviation is $\text{rms}_{\text{PNs}} = 1390 \text{ km s}^{-1}$. The distribution is highly non Gaussian and dominated by several individual components. The main peak appears in the range of velocities from 2400 to 4400 km s^{-1} and its maximum is at $\sim 3100 \text{ km s}^{-1}$, within $1\sigma_{\text{Hy}}$ of the systemic velocity of the Hydra I cluster. In the blue filter velocity range there is a secondary peak at $\sim 1800 \text{ km s}^{-1}$ that falls $2-3\sigma_{\text{Hy}}$ from the systemic velocity of Hydra I. This blue peak may contain a few background galaxy contaminants, as discussed in Sect. 5.1 above. Finally a red peak at $\sim 5000 \text{ km s}^{-1}$ within $\sim 2\sigma_{\text{Hy}}$ of the cluster mean velocity is detected in the velocity interval from 4600 to 5400 km s^{-1} , and there are some PNs with even higher LOS velocities.

The spatial distribution of the PNs – The locations of the detected PNs on the sky are shown in the right panel of Fig. 1. Their spatial distribution can be characterized as follows:

- most PNs follow an elongated north-south distribution approximately centered on NGC 3311;
- there is no secondary high density concentration around NGC 3309. Only one PN, indicated by the gray symbol in the right plot of Fig. 1, has a combination of velocity and position that are compatible with a PN bound to the halo of NGC 3309;
- a possibly separate concentration of PNs is present in the northeastern corner of the field.

We summarize our main results so far:

1. the PN candidates detected in the MSIS field have luminosities consistent with a population of PNs at the distance of the Hydra I cluster;
2. the distribution of PNs in the MSIS field is centered on NGC 3311. Only one candidate is consistent with being bound to NGC 3309, even though NGC 3309 is of comparable luminosity to NGC 3311 and, on account of the X-ray results (see Sect. 2), is likely located in the inner parts of the cluster within the dense ICL, at similar distance from us as NGC 3311;
3. there is no evidence of a single, well-mixed distribution of PNs in the central 100 kpc of the Hydra I cluster, contrary to what one would expect from the dynamically relaxed appearance of the X-ray emission. Instead, the observed PNs separate into three major velocity components.

7. Kinematic substructures and α parameter for the observed PN sample in Hydra I: comparison with a simulated MSIS model

At this point, we would like to reinforce the last point by comparing the observed velocity distribution with a simple model.

² This plot is based on more accurate photometry than and updates Fig. 1 of Ventimiglia et al. (2008).

The model is obtained by assuming a phase-mixed PN population placed at the distance (51 Mpc) and mean recession velocity of NGC 3311, and simulating its line-of-sight velocity distribution by convolving with the MSIS instrumental set up. The velocity dispersion of the PN population is taken to be 464 km s^{-1} , the highest value measured from the long-slit data in Ventimiglia et al. (2010b). In this way we can test more quantitatively whether the observed multi-peaked LOSVD for PNs in our field is biased by the MSIS observational set-up or whether it provides evidence of un-mixed components in the Hydra I cluster core.

7.1. Predicting the luminosity function and LOSVD with MSIS for a model PN population

We first characterize the model in terms of the intrinsic luminosity function and LOSVD of the PN population. Then we describe the steps required to predict the corresponding m_{5007} magnitude vs. LOS velocity diagram and LOSVD that would be measured with the MSIS set up. In the next subsection we compare the results obtained with the observed Hydra I PN sample.

Model for the intrinsic PN population – The intrinsic PNLF can be approximated by the analytical function given by Ciardullo et al. (1989):

$$N(m) = C e^{0.307 m} \left[1 - e^{3(m^* - m)} \right] \quad (4)$$

where m is the observed magnitude, $m^* = 29.0$ is the apparent magnitude of the bright cutoff at the adopted distance of NGC 3311, and C is a multiplicative factor. The integral of $N(m)$ from m^* to $m^* + 8$ gives the total number of PN associated with the bolometric luminosity of the parent stellar population (N_{PN} in Eq. (1)), and the C parameter can be related to the luminosity-specific PN number α (Buzzi et al. 2006). For our model we distribute the magnitudes of a PN population according to a very similar formula fitted by Méndez to the results of Méndez & Soffner (1997).

Next we assume that this PN population is dynamically phase-mixed and that its intrinsic LOSVD is given by a Gaussian centered on the systemic velocity of NGC 3311, \bar{v} ,

$$G(v) = \frac{1}{\sigma_{\text{core}} \sqrt{2\pi}} \exp \left[-\frac{(v - \bar{v})^2}{2\sigma_{\text{core}}^2} \right] \quad (5)$$

where here we adopt $\bar{v} = 3830 \text{ km s}^{-1}$ (Ventimiglia et al. 2010b, corrected to the filter frame), and for the velocity dispersion we take $\sigma_{\text{core}} = 464 \text{ km s}^{-1}$, the highest value measured from the long-slit data in this paper. This approximates the velocity dispersion for the intracluster component in the outer halo of NGC 3311, at central distances $\sim 20\text{--}30 \text{ kpc}$ (Ventimiglia et al. 2010b). We will consider the magnitude-velocity diagram and the LOSVD as histograms in velocity; then in each velocity bin Δv_i , the number of PNs is

$$LF(v_i) \approx N(m) G(v_i) \Delta v_i \quad (6)$$

where $G(v)$ is normalized so that $\sum_i G(v_i) \Delta v_i = 1$.

Simulating the MSIS observations – The magnitude-velocity diagram for such a model population is modified by a number of effects in the MSIS observations, which we simulate as described below. The MSIS simulation procedure implements the following steps:

- the through-slit convolution of the PNLF;
- the convolution with the filter transmission;

- the photometric error convolution;
- the completeness correction;
- the computation of the LOSVD.

The through-slit PNLF – The MSIS technique is a blind survey technique. Therefore the positions of the slits on the sky are not centered on the detected objects, and the further away an object is from the center of its slit, the fainter it becomes. This effect is a function of both seeing and slit width, and it modifies the functional form of the PNLF, which needs to be accounted for when using the LF from MSIS PN detected samples.

In principle, some PNs may be detected in two adjacent slits of the mask, and this would need to be corrected for. However, at the depth of the present Hydra I survey this effect is not important for the predicted PNLF, and indeed no such object has been found in the sample.

Given a “true” PNLF $LF(m)$, the “through slit PNLF” $sLF(m)$ can easily be computed, and depends on slit width and seeing; for further details see Gerhard et al. (2011, in prep.). The effect of the through-slit correction is to shift the $sLF(m)$ faintwards in the observable bright part, compared to the “true” PNLF.

Convolution with filter transmission – When the filter transmission $T(v_i)$ is less than 1 (100%), it shifts the through-slit PNLF to fainter magnitudes. The Δm depends on the value of the filter transmission curve at the wavelength λ or equivalent binned velocity v_i , and is equal to $\Delta m(v_i) = -2.5 \log T(v_i)$. The resulting *instrumental PNLF*, the distribution of source magnitudes before detection, becomes velocity dependent, i.e., $iLF(m, v_i)$.

For the present MSIS Hydra I observations, the combined filter transmission curve from both filters is defined as

$$T(v)_i = \max[T_B(v_i), T_R(v_i)], \quad (7)$$

where B and R denote the blue and red filters. It is 1 where the transmission is 100%, approximately from $\sim 1500 \text{ km s}^{-1}$ to $\sim 3300 \text{ km s}^{-1}$ and from $\sim 4200 \text{ km s}^{-1}$ to $\sim 6300 \text{ km s}^{-1}$; it is < 1 in the filter gap around $\sim 3800 \text{ km s}^{-1}$ and at the low and high velocity ends of the observed range.

Photometric error convolution – Once the instrumental LF $iLF(m, v_i)$ is computed, it must be convolved with the photometric errors which, for the case of the Hydra I observations, are given by the linear function in Eq. (2). Because of the photometric errors, PNs that are intrinsically fainter than the detection limit (here $\text{mag} \sim 30.4$) may be detected if they happen to fall on a positive noise peak on the CCD image, and PNs that are intrinsically brighter than $\text{mag} \sim 30.4$ may be lost from the sample. Generally, because the through-slit PNLF $sLF(m)$ increases towards fainter magnitudes, the photometric errors scatter more faint objects to brighter magnitudes than vice-versa; so the effect of the convolution is to shift the PNLF to brighter magnitudes again.

Completeness correction – The completeness correction at a given observed magnitude is a multiplicative function which accounts for the decreasing fraction of PNs at fainter magnitudes detected against the noise on the MSIS image. For the case at hand it is given in Eq. (3). After the last two steps, we arrive at the final “MSIS PNLF”, $MSLF(m)$ for short.

Computation of the simulated LOSVD – For each velocity bin the $MSLF(m, v_i)$ is integrated between the apparent magnitude of the PNLF bright cut off ($m^* = 29.0$ for Hydra I) and the detection limit magnitude in the relevant filter, $m_{f,\text{dl}}$ (see Sect. 6), to obtain the “observed” cumulative number of PNs in

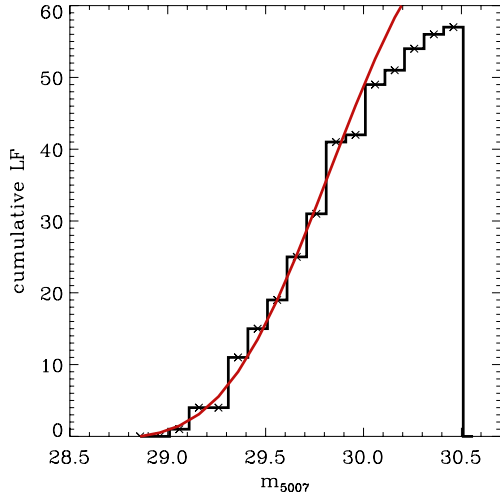


Fig. 2. Cumulative luminosity function predicted for the present MSIS observations and the nominal cutoff magnitude of the Hydra I cluster, 29.0 (full red line, see text), compared with the cumulative histogram of the observed m_{5007} magnitudes.

each velocity bin:

$$N_{\text{MSIS}}(v_i) = \int_{m^*}^{m_{f,dl}} \text{MSLF}(m, v_i) dm. \quad (8)$$

The most cumbersome step in this procedure is the correction for the filter transmission, because it makes the final $\text{MSLF}(m, v_i)$ velocity-dependent. It must correctly be applied *before* the convolution with the photometric errors, because the latter depend on the flux measured at certain positions on the CCD. So the errors on the through-slit magnitudes depend on the filter transmission values of the PNs.

However, we have found that the observed MSLF for the Hydra I PN sample, when obtained from wavelength regions where the filter transmission is $\sim 100\%$, is very similar to the one obtained by summing over the entire filter bandpass. The effect of the velocity dependence on the overall MSLF must therefore be small, and for the comparison of simulated and measured LOSVDs below we have therefore applied the filter transmission only after the error convolution and completeness correction.

Before we discuss the LOSVD obtained from the complete model, we show in Fig. 2 the predicted cumulative luminosity function resulting from error convolution, completeness correction, and filter transmission correction of the through-slit luminosity function, weighting by the number of observed PNs in each velocity bin. Also shown in Fig. 2 is the cumulative histogram of the m_{5007} magnitudes for the 56 observed PNs in the MSIS field. With a cutoff magnitude of 29.0 the model fits the observed histogram fairly well; however, this is not a formal best fit to the distance. The important point shown by Fig. 2 is that the observed MSIS luminosity function of the PN emission sources in the Hydra cluster core is evidently consistent with a population of PNs at ~ 50 Mpc distance.

7.2. Reality of observed kinematic substructures

The simulated MSIS LOSVD given by $N_{\text{MSIS}}(v_i)$ for the simple Gaussian velocity distribution model and luminosity function of Eq. (4) is shown as the green histogram in Fig. 3, with the observed PN LOSVD overplotted in black. The simulated MSIS LOSVD is scaled to approximately match the observed Hydra I sample in the central velocity bins.

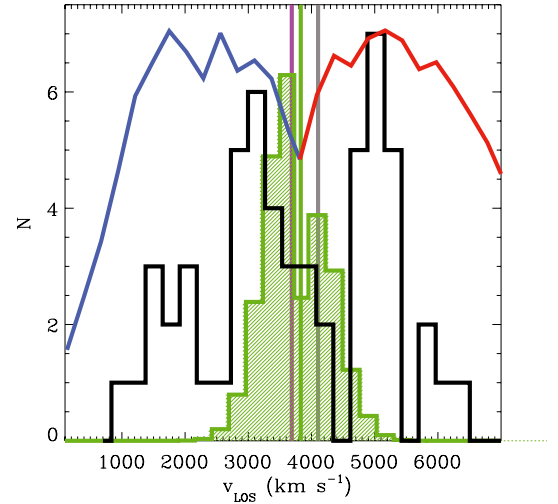


Fig. 3. LOSVD for the Hydra I PN sample from Fig. 1 (black histogram), compared with a simulated MSIS LOSVD (green histogram) for a Gaussian velocity distribution with $\sigma_{\text{core}} = 464 \text{ km s}^{-1}$; see text for further details. The blue-red solid line shows the combined filter transmission curve as given in Eq. (7). The vertical magenta, green and gray lines mark the systemic velocity of Hydra I, NGC 3311 and NGC 3309, respectively.

The comparison between the simulated LOSVD and the Hydra I PN LOSVD in Fig. 3 identifies the central peak at about 3100 km s^{-1} in the observed PN LOSVD with that of the PN population associated with the stellar halo around NGC 3311 in the cluster core, with $\sigma_{\text{core}} \sim 500 \text{ km s}^{-1}$. The mean \bar{v}_{core} and σ_{core} of this component are approximately consistent with those of the intracluster light halo of NGC 3311 derived from the long-slit kinematic analysis in Ventimiglia et al. (2010b). However, the asymmetry and offset of the peak of the observed histogram (by several 100 km s^{-1}) relative to the MSIS convolved model centered at the systemic velocity of NGC 3311 appear significant ($\sigma_{\text{core}} / \sqrt{N_{\text{core}}} \simeq 100 \text{ km s}^{-1}$), arguing for some real asymmetry of the central velocity component. We shall refer to the central peak in the Hydra I PN LOSVD in Fig. 3 as the central ICL component.

Two additional velocity peaks are seen in the LOSVD in Fig. 3, one near 1800 km s^{-1} and one at $\sim 5000 \text{ km s}^{-1}$, which do not have any correspondence with the velocity distribution derived for the simulated MSIS model. These velocity components cannot be explained as artifacts of the MSIS set up, in particular, the filter gap in the $B + R$ filter combination. We will refer to these two velocity components as secondary blue and red peaks, respectively. They reveal the possible presence of two kinematic substructures in the core of Abell 1060, whose origins must be investigated further; see Sect. 8.

7.3. Low α -parameter in the core of Hydra I

We now compare the number of observed PNs with the expectations from the luminosity distribution and kinematics in and around NGC 3311. One issue is the absence of a clear sub-component of PNs with velocity dispersion $\sim 150\text{--}250 \text{ km s}^{-1}$, as would be expected from the central $\sim 25''$ of NGC 3311 (Ventimiglia et al. 2010b). It is known that PN samples in elliptical galaxies are generally not complete in the central regions because of the increasing surface brightness profile; PNs are hard to detect against the image noise in the bright centers. E.g., in observations with the Planetary Nebula

Spectrograph, the threshold surface brightness is typically in the range $\mu_V = 20\text{--}22$ mag/arcsec² (Coccatto et al. 2009). In the current Hydra I data, the PN sample is severely incomplete at $\mu_V = 21.0$ mag/arcsec² (only two PNs are seen at $\mu_V \sim 21.0$ mag/arcsec², and six at $\mu_V \gtrsim 21.5$ mag/arcsec²). Referring to Fig. 13 of Méndez et al. (2001), we estimate that the current sample is not complete for $\mu_V \lesssim 22.0$ mag/arcsec², which is reached at a distance of $\approx 30''$ from the center of NGC 3311 (Arnaboldi et al. 2011, in preparation). At this radius, the projected velocity dispersion has risen to $\sigma_{\text{N3311}}(30'') \approx 300\text{--}400$ km s⁻¹ (Ventimiglia et al. 2010b). Thus the PNs detected in this paper almost exclusively sample the hot (intracluster) halo of NGC 3311. The cold inner galaxy component is not sampled.

The second issue is the observed total number of PNs, given the detection limit, the instrumental set up and the light in NGC 3311 and NGC 3309. Integrating the simulated MSIS luminosity function down to the detection limit of 30.4 mag, we obtain an effective α parameter for our observations of $\alpha_{\text{MSIS,Hy}} = 0.012\alpha_{\text{tot}}$, where α_{tot} quantifies the total number of PNs 8 mag down the PNL³. This value is similar to $\alpha_{0.5}$, the integrated value 0.5 mag down the PNLF. It is consistent with Fig. 1, even though in this figure PNs are seen up to 1.5 mag fainter than the nominal cutoff magnitude, because of (i) the shift towards fainter magnitudes due to the slit losses; and (ii) the completeness correction (Eq. (3)).

We can estimate the bolometric α_{tot} for NGC 3311 from its (FUV-V) color, the relation between (FUV-V) and $\log \alpha_{1.0}$ shown in Fig. 12 of Coccatto et al. (2009), and correcting to $\log \alpha_{\text{tot}}$ by using Fig. 8 of Buzzoni et al. (2006). The (FUV-V) color is determined from the Galex FUV magnitude and the V band magnitude from RC3, both corrected for extinction, as described in Coccatto et al. (2009, Sect. 6.1). The resulting value, (FUV-V)=6.7, corresponds to $\log \alpha_{1.0} = 1.1$ and $\log \alpha_{\text{tot}} = -7.34$. This is very similar to the value of $\log \alpha_{\text{tot}} = -7.30$ found for the Fornax cluster cD galaxy NGC 1399 (Buzzoni et al. 2006). Using the V band light profile of NGC 3311 measured in Arnaboldi et al. (2011, in preparation), and a bolometric correction of 0.85 mag, we can then predict the expected cumulative number of PNs within radius R from the center of NGC 3311. This is shown as the red curve in Fig. 4, after subtracting the luminosity within $20''$ which is not sampled by our MSIS observations. Also shown are the cumulative histograms of the observed number of PNs in the MSIS data, both for all PNs in the field, and for PNs with velocities in the central velocity component only.

Figure 4 shows that the total number of PNs detected in the field falls short of the number predicted from the luminosity profile by a factor ~ 4 . Outside $\sim 100''$, the number of PNs with velocities consistent with the central ICL halo of NGC 3311 is a factor ~ 2 lower than the number of all PNs. Clearly therefore, some of the light at these radii is in a component different from the phase-mixed central ICL halo, but the amount is uncertain because we do not know whether the luminosity-specific α -parameter of this component is similarly low as for the NGC 3311 ICL halo. For example, agreement between observed and predicted PN numbers could be achieved by scaling only the NGC 3311 halo component by a factor ~ 6 . On the other hand, scaling only an outer component will not work, because the discrepancy in Fig. 4 is already seen at small radii. Thus we

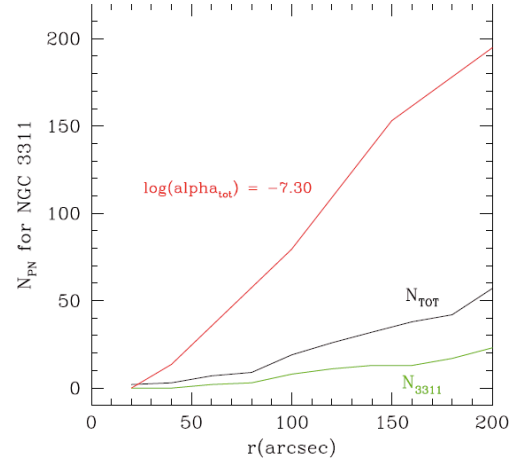


Fig. 4. Observed and predicted cumulative PN numbers, as a function of radial distance from the center of NGC 3311. The green line shows the cumulative number of PNs associated with the central ICL halo of NGC 3311, based on their velocities. The black line shows the cumulative number of all PNs, without velocity selection. The red curve shows the predicted cumulative number of PNs computed using the luminosity-specific parameter α estimated as explained in the text, the MSIS observational set-up, and the integrated bolometric luminosity in increasing circular apertures centered on NGC 3311.

can conclude that the α -parameter of the NGC 3311 ICL halo is low by a factor 4–6.

Such an anomalous specific PN number density requires an explanation. One possibility is that the stellar population in the halo of NGC 3311 is unusually PN poor; this will need studying the stellar population in the galaxy outskirts. A second possibility is that the ram pressure against the hot X-ray emitting gas in the halo of NGC 3311 is high enough to severely shorten the lifetime of the PNs (Dopita et al. 2000; Villaver & Stanghellini 2005). In their simulations, Villaver & Stanghellini (2005) consider a gaseous medium of density $n = 10^{-4}$ cm⁻³ and a relative velocity of 1000 km s⁻¹. They find that the inner PN shell is not significantly affected by the ram pressure stripping during the PN lifetime, and because the inner shell dominates the line emission in their model, the PN visibility lifetime is therefore not shortened relative to an undisturbed PN. However, with a density of the ICM inside $5'$ around NGC 3311 of $\sim 6 \times 10^{-3}$ cm⁻³, and a typical velocity of $\sqrt{3} \times 450$ km s⁻¹ ≈ 800 km s⁻¹ the ram pressure on the NGC 3311 is ~ 40 times stronger than in their simulated case, so the ram pressure effects could be much stronger. Unfortunately, simulations of the evolution of PNs in such dense media are not yet available, to our knowledge.

If this explanation is correct, PNs should be most efficiently ram pressure stripped in the innermost, densest regions of the ICM. Hence in this case we would expect most of the observed PNs to be located in the outermost halo of NGC 3311, even those projected onto the inner parts of our MSIS field. At these outer radii, dynamical time-scales are longer, and phase-mixing should be less complete. This would fit well with the unmixed kinematics and spatial distribution of the observed sample (see also next section).

The third issue is that we do not see a concentration of PNs around NGC 3309. As shown in Sect. 6, only one PN in the sample, shown by the gray symbol in the right panel of Fig. 1, has both position and LOS velocity compatible with being bound to NGC 3309. Whereas using the relative total luminosities of NGC 3309 and NGC 3311 to scale the number of PNs associated with the main LOS velocity component for NGC 3311 in

³ This value includes the light between adjacent slits for the normalization.

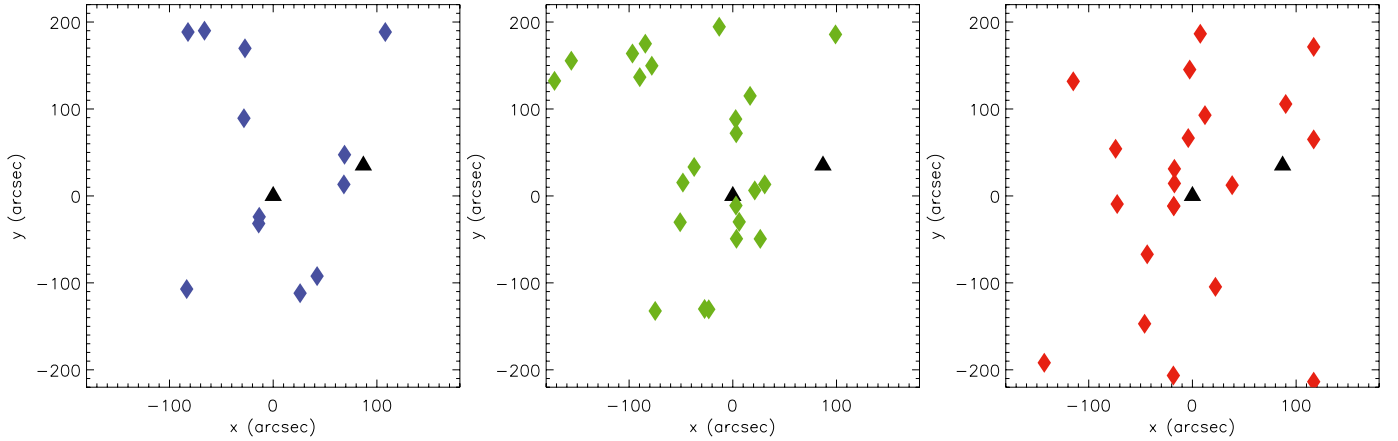


Fig. 5. *Left panel:* spatial distribution of the PNs associated with the blue secondary peak in the PN LOSVD ($<2800 \text{ km s}^{-1}$). *Central panel:* spatial distribution of the PNs associated with the central ICL component (2800 km s^{-1} to 4450 km s^{-1}). *Right panel:* spatial distribution of the PNs associated with the secondary red peak at $>4450 \text{ km s}^{-1}$ in the PN LOSVD. The black triangles indicate NGC 3311 (*center*) and NGC 3309 (north-west of center), respectively. North is up and east is to the left.

Fig. 3 (i.e., 27 PNs), we would expect about 11 PNs associated with the light of NGC 3309 if both galaxies were at the same distance. There are two possible explanations for this fact. One is that NGC 3309 is at significantly larger distance than NGC 3311, such that even PNs at the bright cutoff would be difficult to see. However, a simple calculation shows that then NGC 3309 would be put at $\sim 70 \text{ Mpc}$ well outside the cluster, at variance with X-ray observations finding that its gas atmosphere is confined by the ICM pressure (see Sect. 2). The second possibility is that, similarly as for NGC 3311, also the PNs in NGC 3309 may be severely ram pressure stripped by the galaxy's motion through the dense ICM in the cluster core. This would require that NGC 3309 moves rapidly through the cluster core, and is physically rather close to NGC 3311. Again simulations would be needed to check this quantitatively.

8. The substructures in the Hydra I cluster core

We now turn to a more general discussion of the spatial distribution and kinematics of PNs and galaxies in the central region of the cluster. ICL is believed to originate from galaxies, so it is interesting to ask whether the phase-space substructures seen in the distribution of the PNs that trace the ICL has some correspondence to similar structures in the distribution of cluster galaxies. Thus we want to investigate the spatial distributions of the PNs associated with the velocity subcomponents in the PN LOSVD discussed earlier, and compare them with the spatial distribution of Hydra I galaxies in similar velocity intervals. In this way, we may obtain a better understanding of the dynamical evolution of the galaxies in the cluster core, and of the relevance of cluster substructures for the origin of the diffuse cluster light.

8.1. Spatial distributions of the PN velocity components

We first consider the spatial distribution of the PNs associated with the different velocity components in the PN LOSVD. This is shown in the three panels of Fig. 5, divided according to the classification in Sect. 7.2. Each panel covers a region of $6.8 \times 6.8 \text{ arcmin}^2 \approx 100 \times 100 \text{ kpc}^2$ centered on NGC 3311.

PNs associated with the central ICL component (middle panel of Fig. 5) can be divided into two spatial structures. There is a prominent PN group concentrated, as expected, around NGC 3311, and an elongated east-west distribution in the

northern part of the FoV. By contrast, we see a low PN density region in the southern part of the MSIS field.

Such a north/south asymmetry is seen also in the spatial distribution of the galaxies. Figure 6 displays a larger area, $20 \times 20 \text{ arcmin}^2$, which includes the MSIS field studied in this work, as indicated by the orange square. We can see from the two panels (photo, and schematic) that NGC 3311 and NGC 3309 dominate the center of the MSIS field, that there is a high density of bright galaxies in the northern part of the field, but a deficit of galaxies to the south of NGC 3311.

The spatial distribution of the PNs associated with the secondary red peak in the PN LOSVD is shown in the right panel of Fig. 5. It has a north/south elongation, apparently extending further towards the south of NGC 3311 than the central ICL component, with a high density region north/east of NGC 3311.

Finally, the spatial distribution of the PNs associated with the secondary blue component at 1800 km s^{-1} (left panel of Fig. 5) also appears elongated along the north/south direction, but the smaller number of objects in this subsample makes inferring their spatial structure more difficult.

In summary, there is little evidence of a spherically symmetric well-mixed distribution of PNs in the outer halo of NGC 3311 in the cluster core. Several velocity components are seen, and even the central ICL component centered on NGC 3311 shows signs of spatial substructures.

8.2. Spatial and velocity distribution of Hydra I galaxies: comparison with the PNs sample

The spatial distribution of the galaxies from Christlein & Zabludoff (2003); Misgeld et al. (2008) in the central $20 \times 20 \text{ arcmin}^2$ centered on NGC 3311 is shown in Fig. 6. We would like to analyze their phase-space distribution by dividing into the same velocity components as identified in the PN LOSVD. Therefore, in the image on the left the bright galaxies are encircled with the colors of the PN components in Fig. 5, and in the right panel all galaxies in the field are shown schematically as squares and crosses with the same color code for these velocity bins. NGC 3311 and NGC 3309 are marked in the center of the MSIS field (orange square).

In Fig. 7, the left panel shows the velocity distribution of all the galaxies in the $20 \times 20 \text{ arcmin}^2$ region centered on NGC 3311. In the right panel, the velocity histograms for the

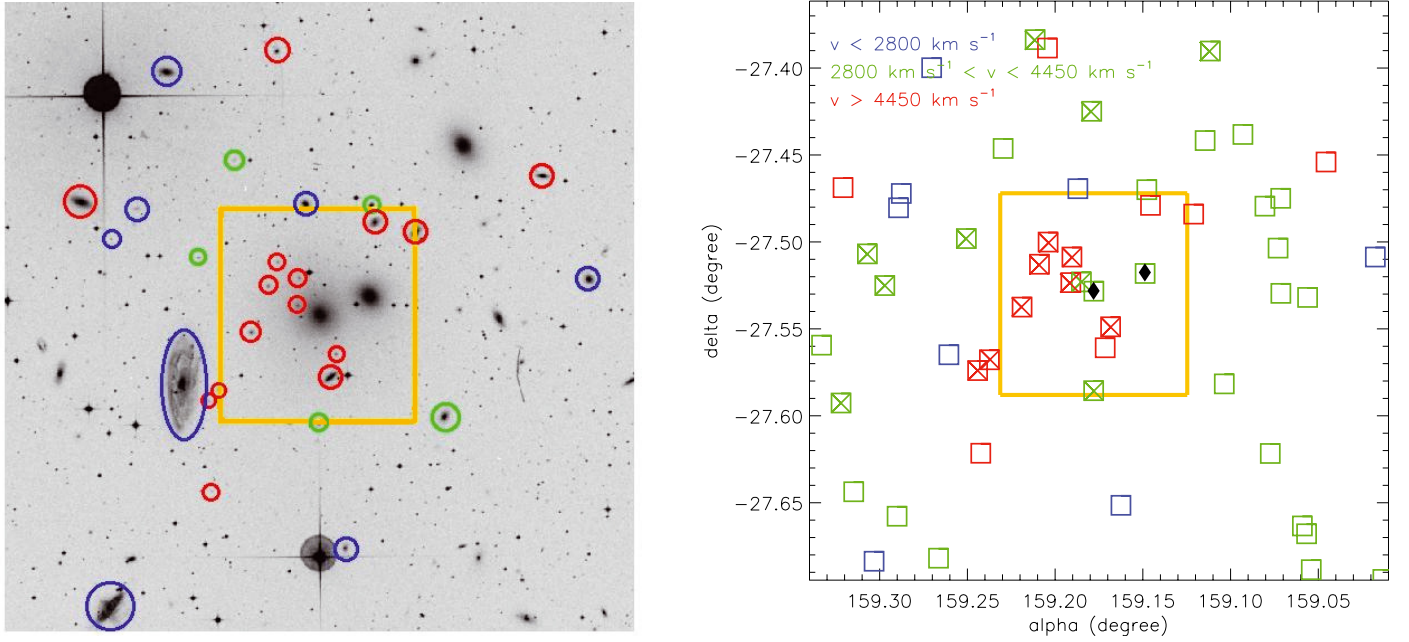


Fig. 6. *Left panel:* 20×20 arcmin² DSS image of the Hydra I cluster. The two bright galaxies at the field center are NGC 3311 (*center*) and NGC 3309 (north-west of center). The blue circles indicate galaxies with $v_{\text{sys}} < 2800$ km s⁻¹, the green circles galaxies with 2800 km s⁻¹ $< v_{\text{sys}} < 4450$ km s⁻¹ (only those within 10 arcmin around NGC 3311 and with $m_R > 15.37$), and the red circles galaxies with $v_{\text{sys}} > 4450$ km s⁻¹. *Right panel:* spatial distribution of Hydra I galaxies in the same area of 20 arcmin² centered on NGC 3311. Squares indicate galaxies from the catalog of Christlein & Zabludoff (2003) and crosses indicate galaxies from Misgeld et al. (2008). The color of the symbols refers to the velocity components in the PN LOSVD as described in Fig. 5. The two diamonds locate NGC 3311 and NGC 3309. The orange square shows the FoV used in the FORS2 MSIS observations.

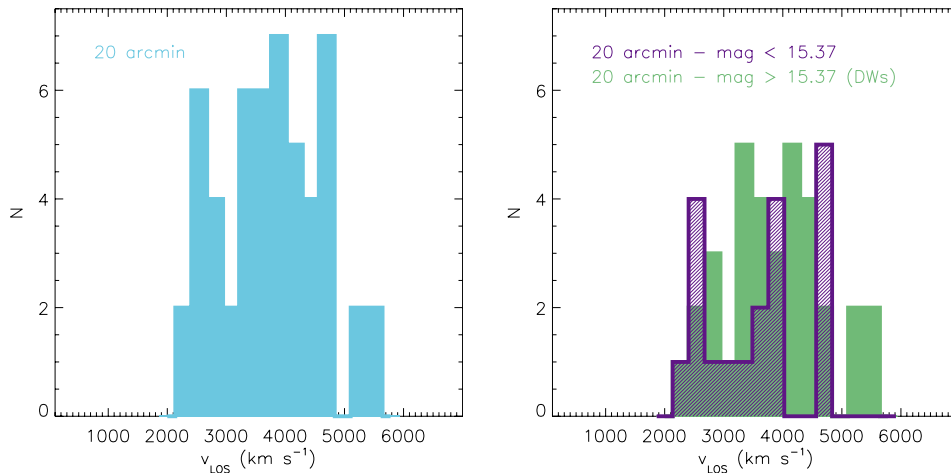


Fig. 7. *Left panel:* histogram showing the LOSVD of all galaxies from the catalog of Christlein & Zabludoff (2003) within an area of 20 arcmin in size centered around NGC 3311. *Right panel:* the purple histogram indicates the LOSVD for the bright galaxies in this field, and the light green histogram the LOSVD for all dwarf galaxies from the catalog of Misgeld et al. (2008) in the same area.

bright galaxies ($m_R < 15.37$, violet color) and dwarf galaxies ($m_R > 15.37$, green color) are shown separately.

The LOSVD for the Hydra I galaxies covers the same velocities as for the PN sample. If we select only galaxies in the range of velocities of the PNs in the central ICL component, from 2800 km s⁻¹ to 4450 km s⁻¹, their LOSVD is consistent with a Gaussian distribution centered at a velocity of 3723 ± 100 km s⁻¹ with a dispersion of 542 ± 80 km s⁻¹. This confirms results from long-slit kinematics in the outer halo of NGC 3311 (Ventimiglia et al. 2010b), where the velocity dispersion was found to increase to ~ 465 km s⁻¹ at $\sim 70''$ radius, 64% of the velocity dispersion of all cluster galaxies.

This subsample of galaxies also has an interesting spatial distribution: the central 6.8×6.8 arcmin² region of the cluster (the MSIS field), while dominated by NGC 3311 and NGC 3309, contains no other Hydra I galaxies with these velocities. Whereas outside this region, they appear uniformly distributed over the field (see the green squares and crosses in the right panel of Fig. 6). NGC 3311 is at the center of the distribution of these galaxies both in space and in velocity. The distribution of these galaxies, as well as the similarity of their velocity dispersion with that measured in the halo of NGC 3311, supports the interpretation of Ventimiglia et al. (2010b) that the halo of NGC 3311 is dominated by intracluster stars that have been torn from galaxies disrupted in the cluster core: galaxies that passed

through the central 100 kpc of the cluster core at modest velocities have all been disrupted.

By contrast, the galaxies with LOS velocities $>4450 \text{ km s}^{-1}$ as in the secondary red peak of the PN LOSVD are mostly located *within* the central $100 \times 100 \text{ kpc}^2$ region of the cluster (red squares and crosses in the right panel of Fig. 6). In this subsample, there are 14 galaxies in total, 5 are classified as bright galaxies and 9 are dwarfs, and 3 bright galaxies and 6 dwarfs fall within the MSIS FORS2 field. These 6 dwarfs are concentrated in the northeastern part of the halo of NGC 3311, in the same region occupied by many PNs associated with the secondary red peak.

Finally, in this region there are only a few galaxies with a LOS velocity lower than 2800 km s^{-1} , compatible with the secondary blue peak in the PNs. They are 8 in total (blue squares and crosses in the right panel of Fig. 6). Only one of these falls on the boundary of the central $100 \times 100 \text{ kpc}^2$ region around NGC 3311. One of these galaxies is the giant spiral NGC 3312, south-east of NGC 3311. The others, including the spiral galaxy NGC 3314, are located at larger distances from NGC 3311.

8.3. Galaxy evolution and presence of substructures in the core of the Hydra I cluster

The distribution of galaxy properties in clusters holds important information on galaxy evolution and the growth of galaxy clusters. In Sect. 8.2, we have discovered an apparent lack of galaxies in the central $100 \times 100 \text{ kpc}^2$ region of the cluster core with velocities in the same range as covered by the cD halo. A similar result has been found in the NGC 5044 group (Mendel et al. 2009). A possible explanation is the tidal disruption of galaxies at small cluster-centric radii. Galaxies with LOS velocities in the range of the central ICL component of the Hydra I cluster are no longer seen in the central region of the cluster, because they were all disrupted in the past during close encounters with the luminous galaxy and the dark matter distribution at the cluster center (Faltenbacher & Mathews 2005). Their former stars now contribute to the diffuse stellar component in the Hydra I core.

Differently from the NGC 5044 group, however, we have found a number of dwarf galaxies *with high velocities* in the Hydra I core, with small cluster-centric radii ($<100 \text{ kpc}$). These dwarfs have LOS velocities higher than 4400 km s^{-1} and seem to form a well defined substructure both in velocity and spatial distribution. We speculate that these galaxies are falling through the cluster core and are not yet disrupted by the tidal interaction with NGC 3311. The PNLF of the subsample of PNs associated spatially and in velocity with this substructure places it almost at the same distance as the central ICL component of the cluster: this group of galaxies may indeed now be on the point of close encounter with NGC 3311 in the cluster center.

Finally, we have found a correlation between the PNs contributing to the secondary blue peak of PN LOSVD, and 8 galaxies with a LOS velocity lower than 2800 km s^{-1} . Among these galaxies is the large spiral galaxy NGC 3312 ($v_{\text{sys}} = 2761 \text{ km s}^{-1}$) as well as NGC 3314 ($v_{\text{sys}} = 2795 \text{ km s}^{-1}$). Fitchett & Merritt (1988) and McMahon et al. (1992) have claimed the presence of a foreground group of galaxies associated with these spirals. Unfortunately due to the small area covered by the current MSIS survey, it is difficult to determine unambiguously whether the low velocity PNs (which from their PNLF are at the distance of the cluster) are associated with these

galaxies. A PN survey covering the region between NGC 3311 and NGC 3312 may provide a definite answer to this question.

9. Summary and conclusions

Using multi-slit imaging spectroscopy with FORS2 on VLT-UT1, we have studied a sample of 56 planetary nebula (PN) candidates in the Hydra I cluster at 50 Mpc distance, targeting a region $100 \times 100 \text{ kpc}^2$ centered on the cluster cD galaxy, NGC 3311. The MSIS technique allows us detect these emission sources and measure their velocities, positions and magnitudes with a single observation.

PN candidates are defined as unresolved emission sources without measurable continuum. Emission sources that are either resolved spatially or in wavelength or have a detected continuum are classified as background galaxies; see Ventimiglia et al. (2010a). We show that the luminosity function of the PN candidates is as expected for a population of PNs at the distance of Hydra I. Moreover, almost all the detected background galaxies occur in the velocity range between 1000 km s^{-1} and 2800 km s^{-1} , blue-shifted by $\geq 900 \text{ km s}^{-1}$ with respect to the mean recession velocity of the Hydra I cluster. From these facts we conclude that any residual contamination of the PN sample by background galaxies with undetectable continuum must be small and restricted to the velocity range given.

The luminosity-specific number density α inferred from the PN sample and the luminosity of diffuse light around NGC 3311 is a factor ~ 4 lower than expected, even if we compare with the low α value determined from the (FUV-V) color which is one of the lowest for elliptical galaxies. A possible interpretation is that ram pressure stripping by the dense, hot X-ray emitting intracluster medium in the center of the cluster core around NGC 3311 dramatically shortens the lifetime of the PN phase. This also seems the most likely explanation for the observed lack of PNs bound to NGC 3309, the other giant elliptical galaxy in the Hydra I core.

The line-of-sight velocity distribution (LOSVD) of the observed PNs shows at least three separate peaks, and their phase-space distribution is inconsistent with a single well-mixed intracluster distribution. One peak, which we term the central intracluster component, is broadly consistent with the outward continuation of the intracluster halo of NGC 3311, which was earlier shown to have a velocity dispersion of $\sim 470 \text{ km s}^{-1}$ at radii of $\geq 50''$ (Ventimiglia et al. 2010b). Simulating MSIS observations for a Gaussian intrinsic LOSVD with $\sim 470 \text{ km s}^{-1}$ centered on the systemic velocity of NGC 3311 has additionally shown significant residual asymmetries, suggesting that also this central component is not completely phase-mixed in the central cluster potential.

Many cluster galaxies are found in the LOS velocity range associated with this central intracluster component (2800 km s^{-1} to 4450 km s^{-1}), but *none* in the central $100 \times 100 \text{ kpc}^2$ around NGC 3311. We suggest that the missing galaxies have been disrupted by the gravitational field of NGC 3311 and the surrounding cluster dark matter, and that their light has been added to the diffuse intracluster halo of NGC 3311 which is traced by the PNs.

The second main peak in the PN LOSVD is centered at 5000 km s^{-1} , some 1200 km s^{-1} to the red of the main component. In the same velocity range, a number of dwarf galaxies are seen, which are projected onto the central $100 \times 100 \text{ kpc}^2$ around NGC 3311 where also the PNs are located. We suggest that the PNs and the galaxies in this red peak of the LOSVD are linked, i.e., on similar orbits through the cluster core, indicating that

the galaxies have been partially disrupted and the tidal debris is traced by the PNs. This will be the subject of a further study based on deep photometry (Arnaboldi et al. 2011, in prep.).

Finally, a third, blue peak in the PN LOSVD is seen at $\sim 1800 \text{ km s}^{-1}$. The spatial distribution of these PNs is elongated in the same sense as for the other two components in the cluster core, but the number of sources with these velocities is smaller and a few of them might be unresolved background galaxies. This makes it difficult to establish a robust association between these PNs and cluster galaxies, such as the group related to the spiral NGC 3312. A larger survey area would be needed to establish such a link.

In summary, from this study of the kinematics of diffuse light in the Hydra I cluster core with PNs, and the comparison with the projected phase-space distribution of galaxies, we infer that: (1) the intracluster stellar population in the Hydra I cluster is not well-mixed, even though this cluster is believed to be the prototype of an evolved and dynamically relaxed cluster based on X-ray indicators; (2) the build-up of diffuse intracluster light and of the cD halo of NGC 3311 are ongoing, through the accretion of material from galaxies falling into the cluster core and tidally interacting with its potential well.

Acknowledgements. The authors thank the ESO VLT staff for their support during the MSIS observations. They also thank L. Coccato, K.C. Freeman and E. Iodice for useful discussions. This research has made use of the Gemini data archive and the NASA/IPAC Extragalactic Database (NED) operated by the Jet Propulsion Laboratory, California Institute of Technology.

References

- Adami, C., Slezak, E., Durret, F., et al. 2005, *A&A*, 429, 39
Agueri, J. A. L., Gerhard, O. E., Arnaboldi, M., et al. 2005, *AJ*, 129, 2585
Arnaboldi, M., & Gerhard, O. 2010, [arXiv:1001.3523]
Arnaboldi, M., Gerhard, O., Aguerri, J. A. L., et al. 2004, *ApJ*, 614, L33
Arnaboldi, M., Gerhard, O., Okamura, S., et al. 2007, *PASJ*, 59, 419
Arnaboldi, M., Doherty, M., Gerhard, O., et al. 2008, *ApJ*, 674, L17
Buzzoni, A., Arnaboldi, M., & Corradi, R. L. M. 2006, *MNRAS*, 368, 877
Castro-Rodríguez, N., Arnaboldi, M., Aguerri, J. A. L., et al. 2009, *A&A*, 507, 621
Christlein, D., & Zabludoff, A. I. 2003, *ApJ*, 591, 764
Ciardullo, R., Jacoby, G. H., Ford, H. C., & Neill, J. D. 1989, *ApJ*, 339, 53
Ciardullo, R., Jacoby, G. H., Feldmeier, J. J., & Bartlett, R. E. 1998, *ApJ*, 492, 62
Ciardullo, R., Sigurdsson, S., Feldmeier, J. J., & Jacoby, G. H. 2005, *ApJ*, 629, 499
Coccato, L., Gerhard, O., Arnaboldi, M., et al. 2009, *MNRAS*, 394, 1249
Coccato, L., Arnaboldi, M., Gerhard, O., et al. 2010, *A&A*, 519, A95
Doherty, M., Arnaboldi, M., Das, P., et al. 2009, *A&A*, 502, 771
Dolag, K., Murante, G., & Borgani, S. 2010, *MNRAS*, 405, 1544
Dopita, M. A., Massaglia, S., Bodo, G., Arnaboldi, M., & Merluzzi, P. 2000, in *Asymmetrical Planetary Nebulae II: From Origins to Microstructures*, ed. J. H. Kastner, N. Soker, & S. Rappaport, ASP Conf. Ser., 199, 423
Durrell, P. R., Ciardullo, R., Feldmeier, J. J., Jacoby, G. H., & Sigurdsson, S. 2002, *ApJ*, 570, 119
Faltenbacher, A., & Mathews, W. G. 2005, *MNRAS*, 362, 498
Feldmeier, J. J., Ciardullo, R., Jacoby, G. H., & Durrell, P. R. 2004, *ApJ*, 615, 196
Fitchett, M., & Merritt, D. 1988, *ApJ*, 335, 18
Furusho, T., Yamasaki, N. Y., Ohashi, T. S. R., et al. 2001, *PASJ*, 53, 421
Gal-Yam, A., Maoz, D., Guhathakurta, P., & Filippenko, A. V. 2003, *AJ*, 125, 1087
Gerhard, O., Arnaboldi, M., Freeman, K. C., et al. 2005, *ApJ*, 621, L93
Gerhard, O., Arnaboldi, M., Freeman, K. C., et al. 2007, *A&A*, 468, 815
Gnedin, O. Y. 2003, *ApJ*, 589, 752
Gonzalez, A. H., Zabludoff, A. I., & Zaritsky, D. 2005, *ApJ*, 618, 195
Hausman, M. A., & Ostriker, J. P. 1978, *ApJ*, 224, 320
Hayakawa, A., Furusho, T., Yamasaki, N. Y., Ishida, M., & Ohashi, T. 2004, *PASJ*, 56, 743
Hayakawa, A., Hoshino, A., Ishida, M., et al. 2006, *PASJ*, 58, 695
Henize, K. G., & Westerlund, B. E. 1963, *ApJ*, 137, 747
Herrmann, K. A., Ciardullo, R., Feldmeier, J. J., & Vinciguerra, M. 2008, *ApJ*, 683, 630
Hilker, M. 2002, in *Extragalactic Star Clusters*, ed. D. P. Geisler, E. K. Grebel, & D. Minniti, IAU Symp., 207, 281
Hilker, M. 2003, in *Extragalactic Globular Cluster Systems*, ed. M. Kissler-Patig, 173
Jacoby, G. H. 1980, *ApJS*, 42, 1
Jacoby, G. H. 1989, *ApJ*, 339, 39
Kapferer, W., Schindler, S., Knollmann, S. R., & van Kampen, E. 2010, *A&A*, 516, A41
Kelson, D. D., Zabludoff, A. I., Williams, K. A., et al. 2002, *ApJ*, 576, 720
Krick, J. E., & Bernstein, R. A. 2007, *AJ*, 134, 466
Lee, M. G., Park, H. S., & Hwang, H. S. 2010, *Science*, 328, 334
McMahon, P. M., van Gorkom, J. H., Richter, O., & Ferguson, H. C. 1992, *AJ*, 103, 399
McNeil, E. K., Arnaboldi, M., Freeman, K. C., et al. 2010, *A&A*, 518, A44
Mendel, J. T., Proctor, R. N., Rasmussen, J., Brough, S., & Forbes, D. A. 2009, *MNRAS*, 396, 2103
Mendez, R. H., & Soffner, T. 1997, *A&A*, 321, 898
Méndez, R. H., Riffeser, A., Kudritzki, R.-P., et al. 2001, *ApJ*, 563, 135
Mieske, S., Hilker, M., & Infante, L. 2005, *A&A*, 438, 103
Mihos, J. C., Harding, P., Feldmeier, J., & Morrison, H. 2005, *ApJ*, 631, L41
Misgeld, I., Mieske, S., & Hilker, M. 2008, *A&A*, 486, 697
Moore, B., Katz, N., Lake, G., Dressler, A., & Oemler, A. 1996, *Nature*, 379, 613
Napolitano, N. R., Pannella, M., Arnaboldi, M., et al. 2003, *ApJ*, 594, 172
Murante, G., Giovalini, M., Gerhard, O., et al. 2007, *MNRAS*, 377, 2
Neill, J. D., Shara, M. M., & Oegerle, W. R. 2005, *ApJ*, 618, 692
Pierini, D., Zibetti, S., Braglia, F., et al. 2008, *A&A*, 483, 727
Puchwein, E., Springel, V., Sijacki, D., & Dolag, K. 2010, *MNRAS*, 406, 936
Renzini, A., & Buzzoni, A. 1986, in *Spectral Evolution of Galaxies*, ed. C. Chiosi, & A. Renzini, Astrophysics and Space Science Library, 122, 195
Richstone, D. O. 1976, *ApJ*, 204, 642
Rudick, C. S., Mihos, J. C., & McBride, C. 2006, *ApJ*, 648, 936
Rudick, C. S., Mihos, J. C., Frey, L. H., & McBride, C. K. 2009, *ApJ*, 699, 1518
Sato, K., Yamasaki, N. Y., Ishida, M., et al. 2007, *PASJ*, 59, 299
Tamura, T., Makishima, K., Fukazawa, Y., Ikebe, Y., & Xu, H. 2000, *ApJ*, 535, 602
Vasterberg, A. R., Lindblad, P. O., & Jorsater, S. 1991, *A&A*, 247, 335
Ventimiglia, G., Arnaboldi, M., & Gerhard, O. 2008, *Astron. Nachr.*, 329, 1057
Ventimiglia, G., Arnaboldi, M., & Gerhard, O. 2010a, *La Rivista del Nuovo Cimento*, in press
Ventimiglia, G., Gerhard, O., Arnaboldi, M., & Coccato, L. 2010b, *A&A*, 520, L9
Villaver, E., & Stanghellini, L. 2005, *ApJ*, 632, 854
Willman, B., Governato, F., Wadsley, J., & Quinn, T. 2004, *MNRAS*, 355, 159
Williams, B. F., Ciardullo, R., Durrell, P. R., et al. 2007, *ApJ*, 656, 756
Yamasaki, N. Y., Ohashi, T., & Furusho, T. 2002, *ApJ*, 578, 833
Zibetti, S., White, S. D. M., Schneider, D. P., & Brinkmann, J. 2005, *MNRAS*, 358, 949